Hydrothermal Microwave Synthesis of Co_3O_4/In_2O_3 Nanostructures for Photoelectrocatalytic Reduction of Cr(VI)

JieJie Nan,[a] Sijia Guo[a], Dalal Alhashmialameer,[b] Qingming He,[a] Yinuo Meng,[a] Ruixiang Ge,[a,*] Salah M. El-Bahy,[c], Nithesh Naik,[d] Vignesh Murugadoss,[e] Mina Huang,[c,f] Ben Bin Xu,[g] Qian Shao,[a,*] Zhanhu Guo [e,*]

[a] College of Chemical and Biological Engineering, Shandong University of Science and Technology, Qingdao 266590, China

[b] Department of Chemistry, College of Science, Taif University, P.O.Box 11099, Taif 21944, Saudi Arabia

[c]Department of Chemistry, Turabah University College, Taif University, P.O.Box 11099, Taif 21944, Saudi Arabia

[d]Department of Mechanical & Manufacturing Engineering, Manipal Institute of Technology, Manipal Academy of Higher Education, Manipal-576104, Karnataka, India

[e] Integrated Composites Laboratory (ICL), Department of Chemical and Bimolecular Engineering, University of Tennessee, Knoxville, TN, 37996, USA

[f] College of Materials Science and Engineering, Taiyuan University of Science and Technology, Taiyuan, 030024, China

[g] Department of Mechanical and Construction Engineering, Faculty of Engineering and Environment, Northumbria University, Newcastle upon Tyne, NE1 8ST, UK

*Corresponding authors: ruixiang_ge@sina.com (R. Ge); shaoqian@sdust.edu.cn.com (Q. Shao); zguo10@utk.edu or nanomaterials2000@gmail.com (Z. Guo)

Abstract

Co_3O_4/In_2O_3 nanocomposites were prepared via a microwave-hydrothermal method and directly used as photoanodes for the photoelectrocatalytic (PEC) process to reduce Cr(VI). The as-prepared Co_3O_4/In_2O_3 composites show a rod-like structure, which is composed of nanoparticles. The PEC experiments indicated that after 120 min of irradiation with 0.7 V bias voltage and visible light, the Cr(VI) reduction efficiency of Co_3O_4/In_2O_3 composites in aqueous solution was 100%, which was superior to the samples prepared by other methods. Moreover, the Co_3O_4/In_2O_3 composite still had a high catalytic activity after five runs of PEC experiments. Elimination experiments demonstrate that photo-generated electrons (e^-) performed a key role in the catalytic reduction of Cr(VI). The significantly improved PEC performance can be attributed to the bias voltage and the p-n heterojunction formed between Co_3O_4 and In_2O_3. Therefore, Co_3O_4/In_2O_3 nanocomposites have a considerable potential for the PEC reduction of Cr(VI).

Keywords: PEC, Microwave-hydrothermal, Co_3O_4/In_2O_3, p-n heterojunction, Reduction of Cr(VI)

1. Introduction

To satisfy the desire for multifunctions and lightweight of the materials and devices,[1] many intractable problems have been created, such as energy shortages[2, 3] and environmental pollution.[4] Although water quality has been improved over the years, heavy metals[5], dyes[6], oil spills[7] and other pollutants discharged from industrial wastewater have caused irrevocable damages to humans and others. For example, chromium (Cr) shows harmful effects due to its toxicity and non-biodegradability.[8] It is normally present in the form of Cr(III) or Cr(VI). Cr(VI) is toxic and mutagenic to organisms, while trivalent chromium is one of the essential trace elements for humans. Traditional chromium removal methods, such as electrocoagulation, membrane separation, reverse osmosis, ion exchange, and chemical precipitation, are limited by incomplete precipitation or high operating costs and cannot effectively remove Cr(VI) ions.[9] To protect and improve the environmental conditions, biodegradation, physical adsorption, photocatalytic and photoelectrocatalytic (PEC) have been widely used in industrial wastewater treatment.[10] Photoelectrocatalysis can directly utilize solar energy to degrade various pollutants in water or the environment in an economical and environmentally friendly manner. Combining photochemical and electrolytic reactions, semiconductor-based PEC have attracted widespread attention in environmental protection.[11]

Among the reported various transition metal oxides such as TiO_2,[12] and ZrO_2,[13] Co_3O_4, as a p-type semiconductor with effective electrons and magnetic properties,[14] is considered as the

most universal oxide material for catalytic applications. Indium oxide (In_2O_3) is an n-type semiconductor that has superior electrical conductivity and excellent photoelectrochemical stability. Up to now, In_2O_3 nanorods, nanoribbons, and nanowires have been prepared to supply a greater specific surface area for reinforced photoelectrochemical reactions.[15] P-CuO-N-In_2O_3 quantum dot heterojunction photocatalysts for long-wavelength visible light photocatalysis were reported.[16] Dai *et al.* investigated the synthesis of nanocrystalline In_2O_3 and reported its photocatalytic properties.[17] Zhang *et al*. reported Co_3O_4 nanoparticles and graphene in synergistic effect as catalysts for the degradation of Orange II dye.[18] The association of Co_3O_4 nanoparticles and the graphene sheets was reported to provide superior catalytic performance over pure Co_3O_4. Wang *et al*. synthesized nanostructured two-component cobalt metal titanate and cobalt oxide, which degraded azo dyes effectively under 250W mercury light irradiation.[19] Recently, some attempts have been made to promote the catalytic efficiency of Co_3O_4.[20] To make oxide semiconductors sensitive to visible light and to raise the electronic-hole pair separation efficiency, the semiconductor was assembled with designed materials to form heterojunctions. Prior studies reported the preparation of Ag_3PO_4/Co_3O_4 heterojunction photocatalysts for the degradation of rhodamine B by a simple precipitation method.[21] Huang *et al*. synthesized efficient $Co_3O_4/CdIn_2S_4$ heterojunction photocatalysts to enhance the photocatalytic CO_2 reduction reaction efficiency.[22]

Among the types of studied heterojunctions, the internal electric field of p-n heterojunctions is extensively utilized to foster the migration and separation of photogenerated carriers, such as

in solar cells and photocatalytic systems. The Co_3O_4/In_2O_3 composite catalysts have drawn much focus in recent years due to their good visible light response activity and p-n heterojunction structure,[23] and higher photogenerated electron-hole separation efficiency than single Co_3O_4 catalysts. For example, Yang *et al*. synthesized In_2O_3/Co_3O_4 composite for over ultra-low temperature Co oxidation.[24] Shi *et al*. reported that p-n heterojunction between Co_3O_4 and In_2O_3 played an important role in triethylamine sensing.[23] It has been reported that Co_3O_4 has the potential to act as a catalyst for photoelectrochemical water oxidation in visible light.[25] Owing to the synergistic reaction between n-type and p-type semiconductors, the catalytic activity will be significantly improved. Consequently, the combination of Co_3O_4 and In_2O_3 can successfully construct p-n heterostructures with built-in charge fields. In addition, the p-n heterojunction at the boundary between Co_3O_4 and In_2O_3 further improves the charged separation efficiency.

Photoelectrocatalysis is a photocatalytic oxidation technology enhanced by photoelectric synergy, which can effectively facilitate the separation of photogenerated electrons from holes.[26] Unlike photocatalytic, PEC reaction requires a bias voltage to facilitate the effective export of photogenerated electrons from the outer loop and diminish the chance of electron-hole complexation, thereby increasing the photocatalytic reaction rate. Xu *et al.* prepared the In_2O_3/Co_3O_4 pozzolanic composites using In/Co-MOFs pyrolysis and demonstrated the efficient photocatalytic degradation of tetracycline and methylene blue.[27] In recent years, there have been many studies on Co_3O_4/In_2O_3 heterojunction structures as gas sensor elements. However, there are few studies on the PEC degradation of pollutants in water based on Co_3O_4/In_2O_3 p-n

heterojunction structure.

In this study, Co_3O_4/In_2O_3 composites with a heterojunction structure were fabricate via a microwave-hydrothermal method. Compared with solvothermal and co-precipitation methods, the microwave-hydrothermal method exhibits the advantages of shorter reaction time and higher yields of the product. Owing to the presence of Cr(VI) mainly as $Cr_2O_7^{2-}$ in water, $K_2Cr_2O_7$ solution was utilized to simulate Cr(VI)-containing wastewater. The experimental results demonstrated that the synthesized Co_3O_4/In_2O_3 composites displayed a significantly enhanced PEC activity for Cr(VI) reduction than pure Co_3O_4 and In_2O_3 particles. Meanwhile, the stability and reusability of Co_3O_4/In_2O_3 composites were investigated by cycling experiments. In addition, the reaction mechanism was also confirmed by various characterization techniques such as radical trapping experiments and Mott-Schottky (MTS). This study provides a theoretical basis for the utilization of PEC reduction of Cr(VI) in wastewater.

2. Experimental

2.1. Preparation of catalysts

To prepare the Co_3O_4/In_2O_3 nanocomposites, InCo bimetallic precursors were firstly synthesized via a microwave-hydrothermal method. In brief, 1.455 g of $Co(NO_3)_2{\cdot}6H_2O$, a certain amount of $In(NO_3)_3{\cdot}4.5H_2O$, and 1.8 g of $CO(NH_2)_2$ were dissolved by 50 mL deionized water, forming a clear metal salt solution. The In/Co molar ratios were set to be 0.03:1, 0.05:1, and 0.07:1, respectively. The resulting solution was then transferred to a microwave-hydrothermal parallel synthesizer (Beijing XiangHu Science and Technology

Development Co., Ltd, XH-800S, China). By applying a microwave power of 1000 W, the reaction temperature was raised to 120 °C within 30 minutes. After hydrothermal reaction at 120 °C for 2 h, purple precursors were collected, and were washed and dried for further use. To convert the precursors into the Co_3O_4/In_2O_3 nanocomposites, the as-prepared precursors were calcined in a muffle furnace for 2 h at a certain temperature (i.e., T=350, 400, 450, 500, and 550 °C). The as-prepared samples are labeled as CI-M-T, where M is the In/Co molar ratio and T is the calcination temperature. The detailed information of the samples, such as the In/Co molar ratio, the needed amount of the materials and the abbreviations, are listed in Table S1. For comparison, pure Co_3O_4 and In_2O_3 particles were prepared via similar methods, except for the absence of $In(NO_3)_3 \cdot 4.5H_2O$ or $Co(NO_3)_2 \cdot 6H_2O$ in the metal salt solution.

2.2. Preparation of PEC electrode

The PEC electrode was prepared by a drop-casting method. In brief, 30 mg of catalyst, 15 mg of PTFE, and 6 mg of acetylene black were dispersed in 1 mL ethanol after ultrasonic treatment for 15 min. The mixture was subsequently coated on a piece of nickel foam (2 × 2 cm^2). After drying at 60 °C for 12 hours,[28] the nickel foam loaded with the active substance was weighed and the difference in mass before and after drop-casting was the loading mass of the sample. The current density was calculated based on the geometric area of nickel foam electrode (2 × 2 cm^2). The thickness of the nickel foam was 0.5 mm and was supplied by the manufacturer, Suzhou Shengnuo Technology Company Limited.

2.3. PEC performance tests

The PEC performances were evaluated via a previously reported method with minor

modifications.[29] Please see the Supporting Information for details.

3. Results and discussion

3.1. Preparation and characterization

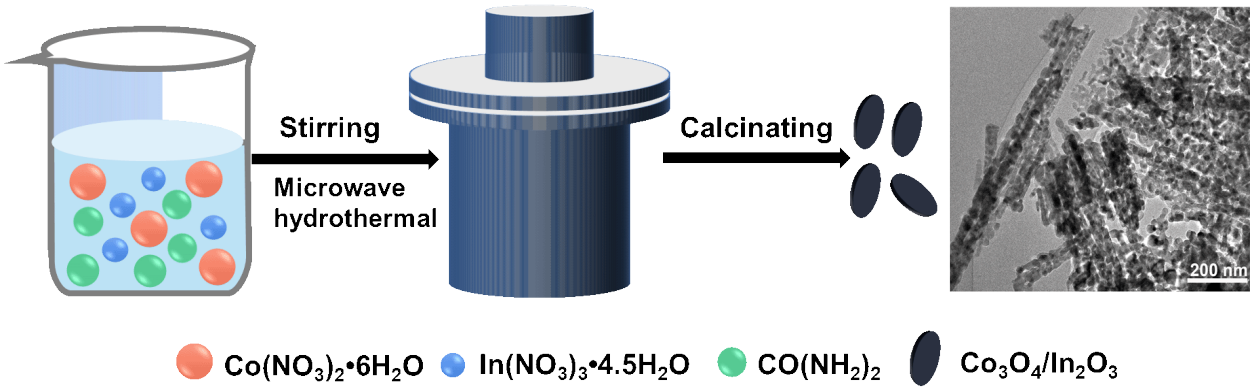

Scheme 1. Synthetic route for Co_3O_4/In_2O_3 composites.

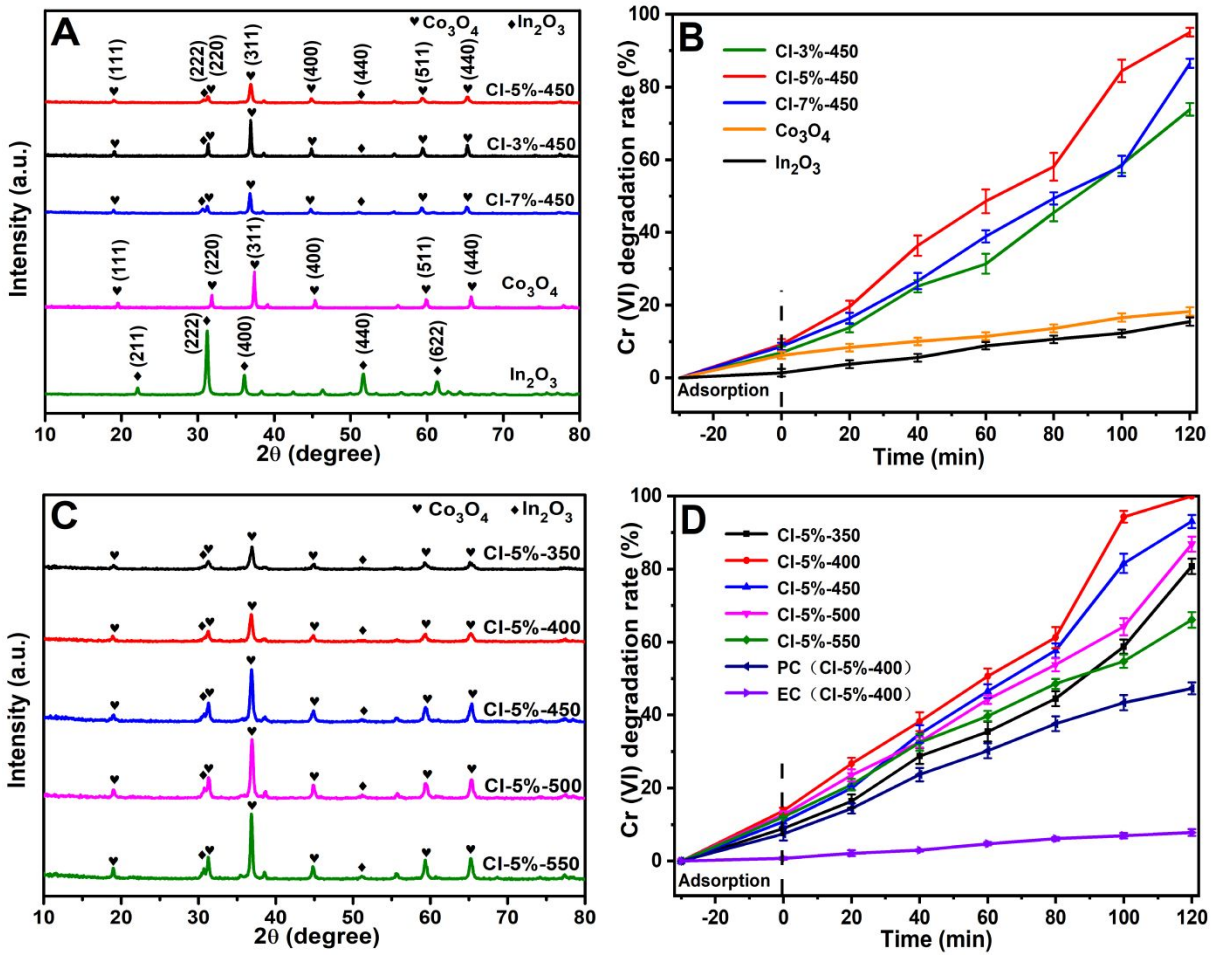

Figure 1. (A) XRD patterns and (B) PEC reduction efficiency of Cr(VI) under 0.7 V bias voltage and visible light irradiation of the samples with different In/Co molar ratios and Co_3O_4 and In_2O_3 particles; (C) XRD patterns and (D) PEC efficiency of Cr(VI) under 0.7 V bias voltage and visible light irradiation of the samples prepared at different calcination temperatures and photocatalytic and electrocatalytic reduction efficiency of Cr (VI) of Co_3O_4/In_2O_3 composites.

As shown in scheme 1, the Co_3O_4/In_2O_3 composites were prepared by a microwave-hydrothermal method and a subsequent calcination process. To screen out the optimal In_2O_3 content, a series of Co_3O_4/In_2O_3 composites with different In/Co molar ratios were prepared, and then their PEC performances were evaluated. The X-ray diffraction patterns of Co_3O_4, In_2O_3, and Co_3O_4/In_2O_3 composites with different In/Co molar ratios are shown in Figure

1A. For the Co_3O_4 sample, the diffraction peaks at 19.1°, 31.3°, 36.9°, 44.7°, 59.4°, and 65.4° can be indexed to the (111), (220), (311), (400), (511) and (440) planes of cubic Co_3O_4 (JCPDS, No. 42-1467), respectively.[30] For the In_2O_3 sample, the five diffraction peaks at 2θ = 21.4°, 30.5°, 35.4°, 51.1°, and 60.7° correspond to the (211), (222), (400), (440) and (622) crystallographic planes of cubic In_2O_3 (JCPDS, NO. 06-0416), respectively.[31] The Co_3O_4/In_2O_3 composites prepared by calcination at 450 °C exhibit all the characteristic peaks of Co_3O_4, as well as the diffraction peaks corresponding to the (222) and (440) planes of In_2O_3. However, in comparison with pure Co_3O_4, the characteristic peaks of Co_3O_4 in the Co_3O_4/In_2O_3 composites shift toward a lower angle, which can be attributed to the higher radius of the In dopant than that of Co atoms from the Co_3O_4 host.[17] The results of the XRD measurement illustrate that the Co_3O_4/In_2O_3 heterojunction structure has been synthesized.

The PEC reduction efficiencies of Cr(VI) for Co_3O_4/In_2O_3 composites with different In/Co molar ratios are shown in Figure 1B. All PEC reduction tests were performed at pH=2 (Please see detailed descriptions in Supporting Information and Figure S1). To eliminate the interference of adsorption, the concentration of Cr(VI) after 30 min of adsorption in the dark was used as the PEC initial concentration. As shown in Figure S2, after 30 minutes, an adsorption-desorption equilibrium for Cr(VI) was establish, and the adsorption amount of Cr(VI) of the tested samples was all less than 14%. The PEC reduction efficiencies of Cr(VI) for Co_3O_4/In_2O_3 composites with different In/Co molar ratios are shown in Figure 1B. It is demonstrated that, under the 0.7 V bias voltage and visible light irradiation, the Cr(VI) PEC reduction efficiencies of different

samples follow an order of CI-5%-450 (95.08%) > CI-7%-450 (86.83%) > CI-3%-450 (73.88%). Consequently, the In/Co molar ratio of 5% was selected for further evaluation.

Next, the influence of calcination temperatures on the Cr(VI) reduction efficiency was investigated. The Co_3O_4/In_2O_3 composites (In/Co molar ratio is 5%) prepared at different calcination temperatures were characterized and their performance were tested. No other impurity peaks appear in the XRD spectra of Co_3O_4/ In_2O_3 (Figure 1C), which indicates that the as-prepared composites have high purity and good crystallinity.[4] With the increase of calcination temperature, the observed sharper diffraction peak is indicative of a larger gain size and a higher degree of crystallinity.[32]

Figure 1D shows the PEC performances of the samples calcined at different temperatures. It was observed that both of photocatalysis and electrocatalysis (0.7V) are inefficient for Cr(VI) reduction, which a low efficiency of only 47.33% and 7.79%, respectively. In sharp contrast, the PEC method delivered high performances, with an optimal Cr(VI) reduction efficiency of 100% being achieved over the CI-5%-400, indicating that the synergistic effect of photocatalysis and electrocatalysis improves the reduction efficiency. Thus, it is demonstrated that the Co_3O_4/In_2O_3 composites (In/Co molar ratio is 5%) prepared at 400 °C show an optimal Cr(VI) reduction performance.

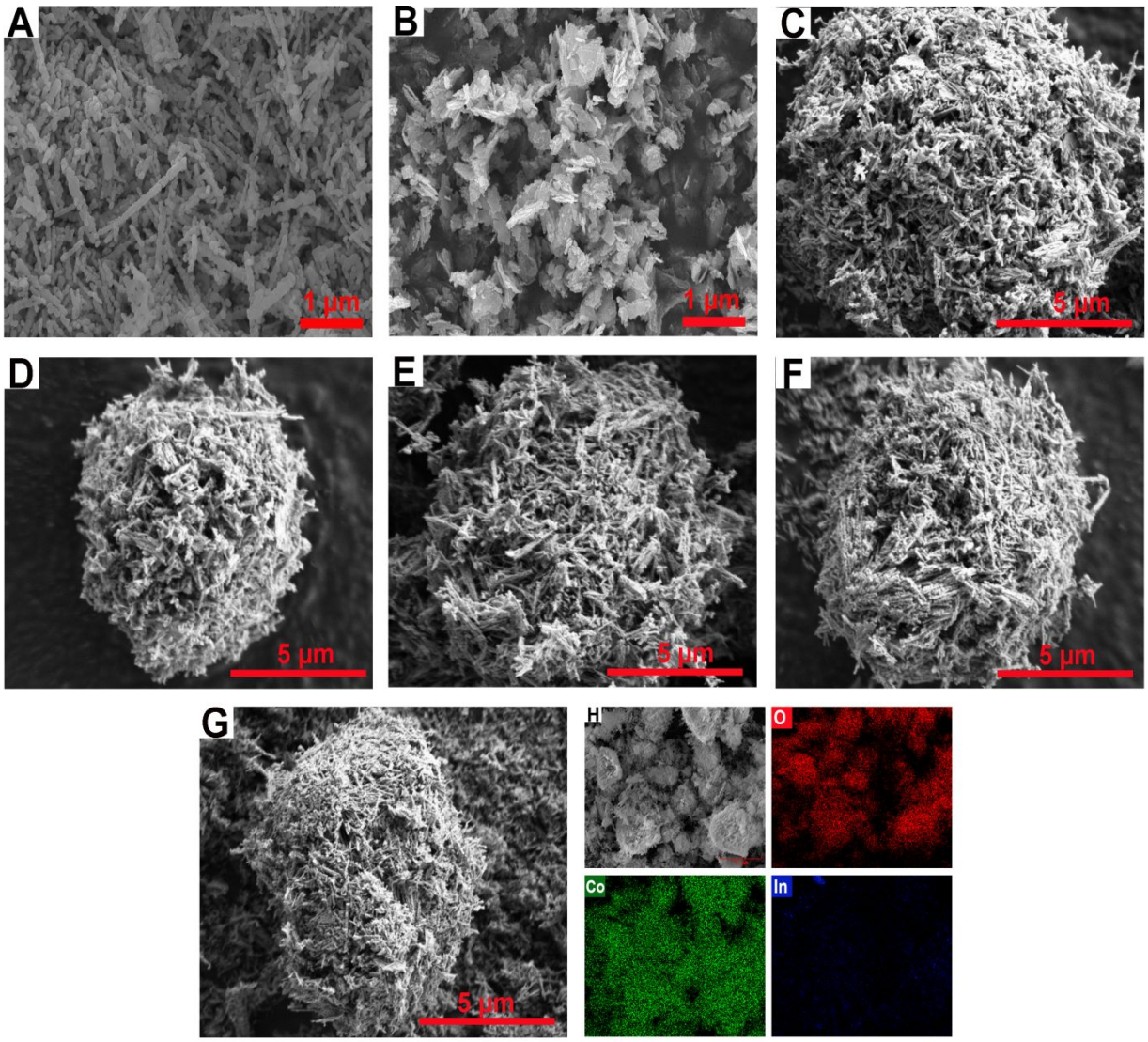

Figure 2. SEM images of (A) Co_3O_4, (B) In_2O_3, (C) CI-5%-350, (D) CI-5%-400, (E) CI-5%-450, (F) CI-5%-500 and (G) CI-5%-550; (H) EDS elemental mapping images of CI-5%-400.

Figures 2A-G display the SEM images of the prepared Co_3O_4, In_2O_3 particles, and Co_3O_4/In_2O_3 composites. As shown in Figure 2A, the Co_3O_4 shows a rod-like morphology, whereas the In_2O_3 consists of irregular porous nanosheets (Figures 2B). Figures 2C-G shows the morphology of the composites at different calcination temperatures. The CI-5%-400 exhibits a rod-like morphology (Figure 2D), and increasing calcination temperature leads to a higher

degree of agglomeration and a more irregular morphology (Figures E-G). This may be attributed to the loss of water molecules and interlayer species of the hydroxide precursor during calcination.[33]

Figure 2H shows the SEM and EDS elemental mapping images of CI-5%-400. It can be seen that O, Co, and In elements are evenly distributed in CI-5%-400. Although the elemental mapping image of In is not clear compared with that of O and Co, which is because the content of In is lower than that of O and Co, it can be concluded that trace amount of indium has been doped in the composites. Furthermore, the SEM-EDS analysis (Figure S3) indicates an In/Co atomic ratio of 0.043 for CI-5%-400, which is in consistence with the feed ratio of In and Co metal salts.[15]

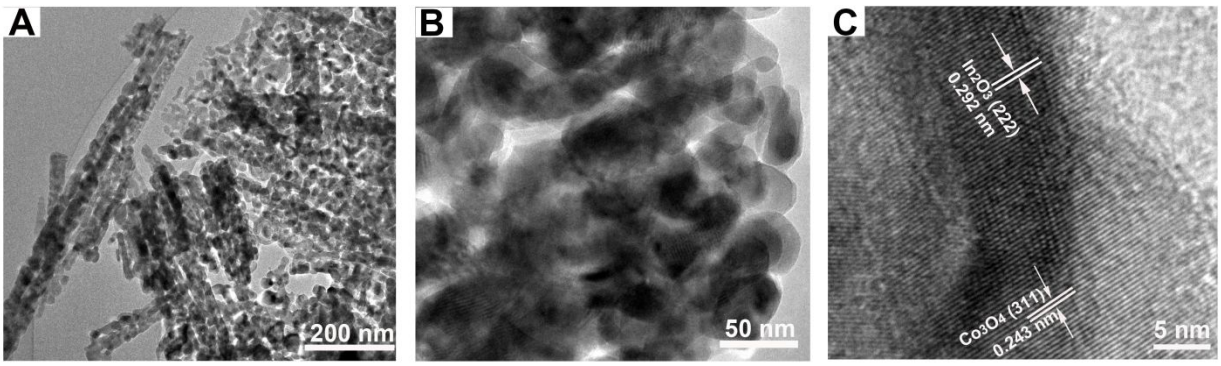

Figure 3. (A-B) TEM images and (C) HRTEM image of CI-5%-400.

The microstructure and morphology of the CI-5%-400 were further characterized by TEM analysis. It reveals that the CI-5%-400 consists of numerous nanoparticles (Figures 3A and B). Moreover, the high-resolution TEM (HRTEM) image of CI-5%-400 shows the clear lattice fringes with an interval of 0.243 and 0.292 nm (Figure 3C), corresponding to the Co_3O_4 (311) and In_2O_3 (222) planes, respectively, [34,35] suggesting a close contact between Co_3O_4 and In_2O_3.

The selected electron diffraction (SAED) patterns of Co_3O_4 and In_2O_3 show the (220), (311), (440), and (222), (400), (440) crystal planes, respectively, demonstrating the successful preparation of the Co_3O_4 and In_2O_3 particles (Figure S4 A,B). Moreover, as shown in Figure S4C, for the CI-5%-400, the SAED exhibits Co_3O_4 (311) and In_2O_3 (222) crystalline planes, which further indicate that Co_3O_4/In_2O_3 composites were successfully prepared. In addition, the CI-5%-400 also exhibits highly crystalline and polycrystalline character (Figure S4C).[36]

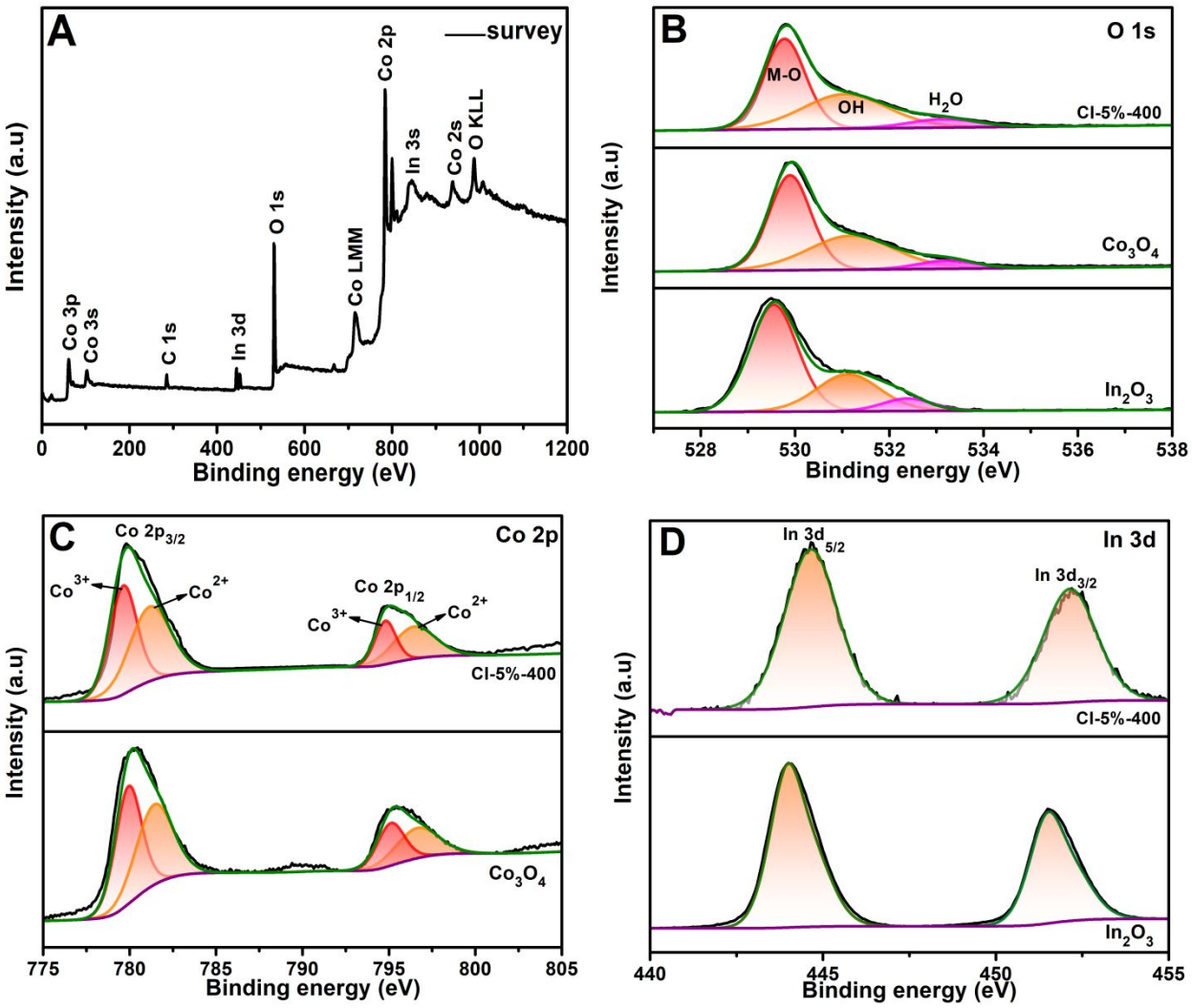

Figure 4. (A) Full survey spectrum of CI-5%-400, (B) the XPS spectra of O 1s of CI-5%-400, Co_3O_4 and

In_2O_3, (C) the XPS spectra of Co 2p of CI-5%-400 and Co_3O_4, (D) the XPS spectra of In 3d of CI-5%-400 and In_2O_3.

The chemical composition and elemental valence states of the catalysts were investigated through XPS measurements.[37] The XPS full survey spectrum of CI-5%-400 is shown in Figure 4A, which shows the presence of Co, In, and O elements.[38] The O 1s spectra (Figure 4B) exhibit three peaks at 529.78, 531.1, and 533.7 eV, which can be attributed to the lattice oxygen (O^{2-}), oxygen vacancy (OH^-) and molecular water (H_2O) species, respectively.[38,39] For Co 2p spectra (Figure 4C), two peaks at 780.2 and 795.3 eV belong to Co $2p_{3/2}$ and Co $2p_{1/2}$, respectively.[40] Furthermore, the difference in binding energy between the Co $2p_{3/2}$ and Co $2p_{1/2}$ orbitals (15.1 eV) suggests the co-existence of cobalt(II) and cobalt(III) species.[41] Moreover, the peaks located at the binding energies of 794.9 and 779.9 eV can be attributed to Co^{3+},[42] and the peaks at 796.8 and 781.6 eV originate from Co^{2+}.[40] The Co^{3+}/Co^{2+} ratio of Co_3O_4/In_2O_3 (1.38) is slightly higher than Co_3O_4 (0.61). Figure 4D displays the In 3d XPS spectra of In_2O_3 and CI-5%-400. The two main peaks at 444.6 and 452.1 eV are attributed to the $3d_{5/2}$ and $3d_{3/2}$ spin orbitals of In,[43] respectively. Compared with pure In_2O_3, the In 3d spectrum of Co_3O_4/In_2O_3 heterojunction shifts toward higher binding energy, indicating a higher valence state of In from Co_3O_4/In_2O_3, which is similar to the literature.[23] On the other hand, there was no significant difference in the valence state of the samples obtained at different calcination temperatures (Figure S5). The above results demonstrate that the electronic structures of Co_3O_4 and In_2O_3 in Co_3O_4/In_2O_3 composites were significantly modified, which might be attributed to the close contact between Co_3O_4 and In_2O_3.

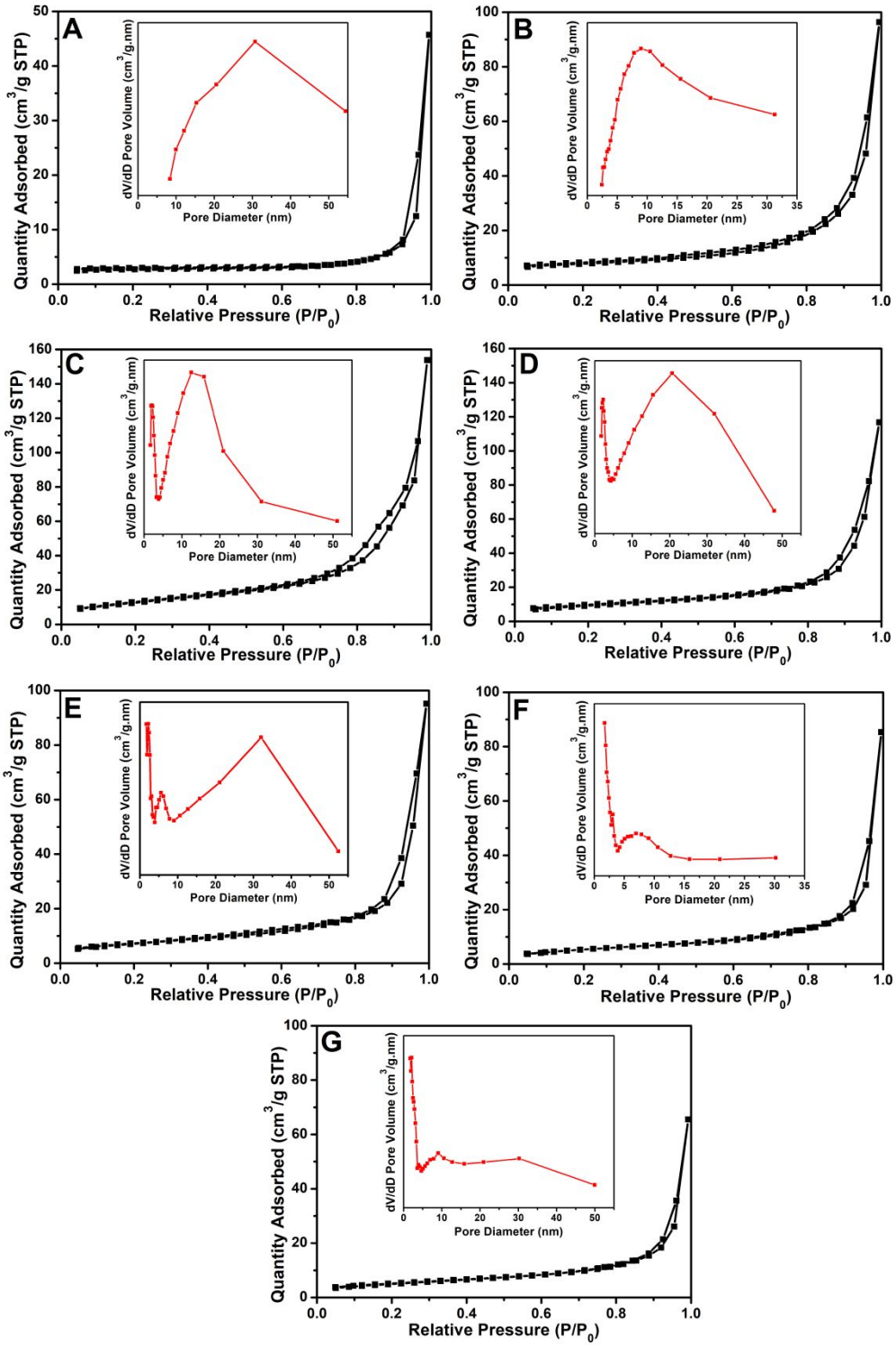

Figure 5. N_2 adsorption−desorption isotherms and pore size distribution curve of samples: (A) Co_3O_4, (B) In_2O_3, (C) CI-5%-350, (D) CI-5%-400, (E) CI-5%-450, (F) CI-5%-500 and (G) CI-5%-550.

The N_2 adsorption-desorption isotherms measurements for the composites prepared at

different calcination temperatures, Co_3O_4, and In_2O_3 particles were carried out. As shown in Figure 5, all the samples exhibit the type IV adsorption isotherms with H3-type hysteresis loops according to the IUPAC classification, which demonstrate the presence of the mesoporous structures.[44] Furthermore, the specific surface area, pore size, and pore volume of all samples are shown in Table S2. The Co_3O_4 and In_2O_3 show a low specific surface area of 9.51 m^2g^{-1}, and 25.76 m^2g^{-1}, and a small pore volume of 0.01 $cm^3g^{-1}$and 0.06 cm^3g^{-1}, respectively. In sharp contrast, the CI-5%-400 exhibits a significant increase in the specific surface area (32.72 m^2g^{-1}) and the pore volume (0.09 cm^3g^{-1}), suggesting that the heterogeneous interfaces between Co_3O_4 and In_2O_3 create more pores and provide a higher specific surface area, which are favorable for exposing more active sites and thus improving the PEC performances.[45] On the other hand, increasing the calcination temperature leads to significantly decreased specific surface areas of Co_3O_4/In_2O_3 composites (Table S2), which may be attributed to a higher degree of agglomeration at higher calcination temperatures,[46] in consistence with XRD and SEM results. Moreover, CI-5%-400 has the largest (10.74 nm) pore size, and the pore size distributions of the samples ranging from of 4-11 nm, which provides an efective transport pathway for the PEC reaction process.

3.2. Optical and electrical properties

The UV-vis diffuse reflectance spectra (DRS) of the as-prepared catalysts within the range of 200-800 nm were measured and were shown in Figure 6A. It is shown that the visible light response range of Co_3O_4/In_2O_3 composites loaded with Co_3O_4 extends from 400 nm to 800 nm.

This can be attributed to the light absorption of Co_3O_4. Meanwhile, the sample CI-5%-400 has a high light absorption intensity, indicating its potential of effectively utilizing visible light energy.

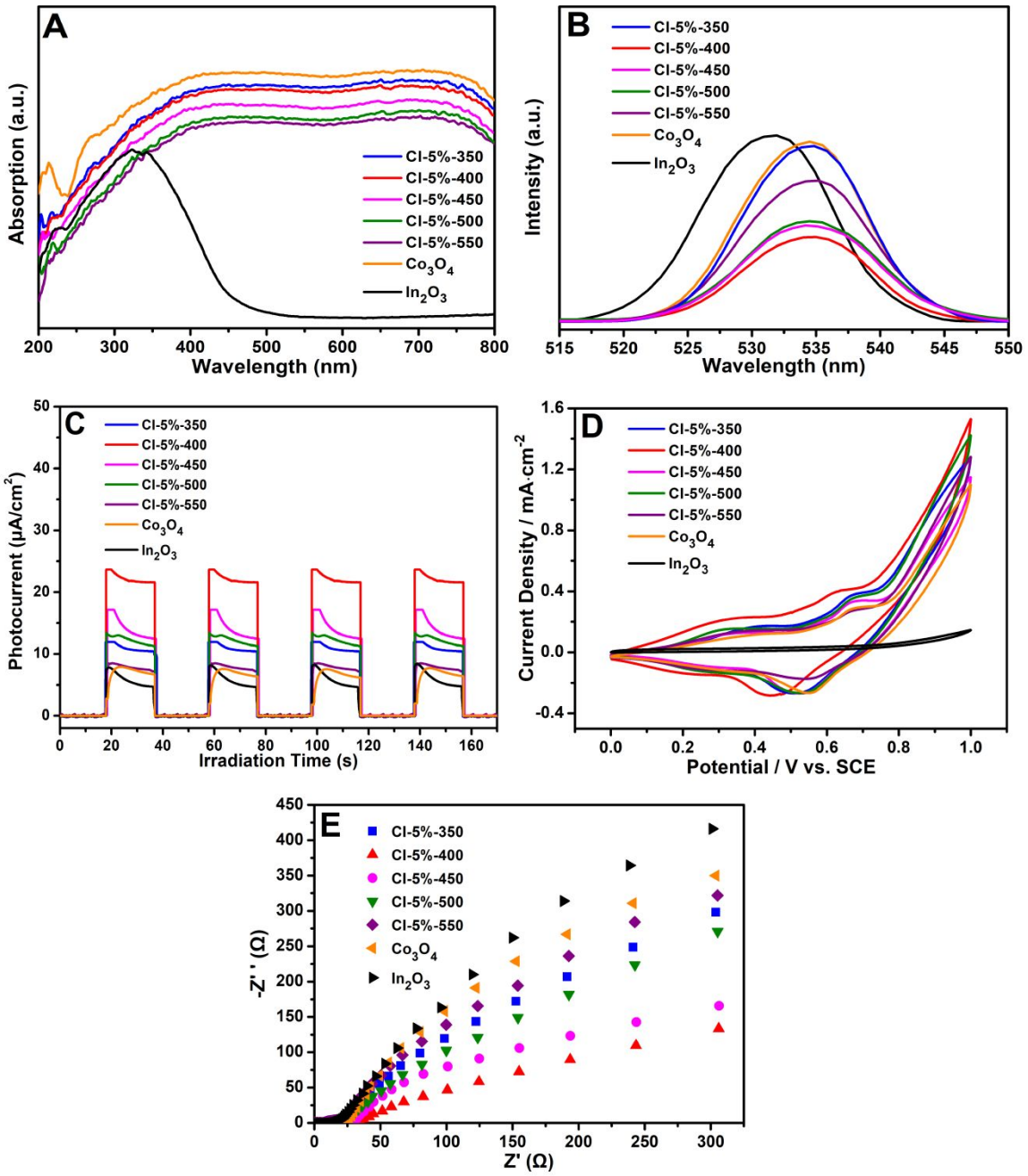

Figure 6. (A) UV-Vis diffuse reflectance spectra, (B) PL spectra, (C) transient photocurrent spectra, (D) CV curves and (E) EIS spectra of Co_3O_4, In_2O_3 particles and Co_3O_4/In_2O_3 composites.

Then photoluminescence (PL) spectroscopy analysis was carried out to provide more

insight into the PEC properties of the samples.[47] Under an excitation wavelength of λ=266 nm, the PL of pure In_2O_3 shows an obvious peak at 530 nm, but the Co_3O_4/In_2O_3 composites showed the similar emission peak intensity to Co_3O_4 due to the consistency in structure and morphology between Co_3O_4/In_2O_3 and Co_3O_4 (Figure 6B). More notably, compared with other synthesized samples, CI-5%-400 has the lowest fluorescence intensity, indicating improved efficiency of the migration and separation of photogenerated electrons-hole, thereby effectively enhancing the PEC activity.[20]

We tested the transient photocurrent responses for all the samples. As shown in Figure 6C, the Co_3O_4/In_2O_3 composites exhibit higher photocurrent densities than In_2O_3 and Co_3O_4, indicating that the heterojunction could produce more charge carriers and advantageously separate electron-hole pairs. Moreover, an optimal photocurrent density was achieved over the CI-5%-400. In order to reveal the electrochemical characteristics, cyclic voltammetry (CV) tests were carried out by using a three-electrode system in Cr(VI) solution (10 mg/L, 100 mL) with a scan rate fixed at 50 mV/s. As shown in Figure 6D, CI-5%-400 delivers a higher current density than Co_3O_4 and In_2O_3 samples, suggesting a better redox activity of the composite catalyst. Furthermore, electrochemical impedance spectroscopy (EIS) was used to further evaluate the charge transfer impedance. As shown in Figure 6E, the CI-5%-400 exhibits the smallest arc radius, which is indicative of a low charge transfer resistance and a fast electron transfer dynamics.[48] These analyses demonstrate that p-n heterojunctions of the CI-5%-400 significantly improve the separation and migration of photogenerated carriers, suggesting a great promise of

the CI-5%-400 as a PEC catalyst.

3.3. Photoelectrocatalytic activity

The catalytic reduction activities of Cr(VI) of CI-5%-400 at different bias voltages (0 -1 V) were investigated. As displayed in Figure 7A, the reduction rate increased sequentially with the increase of bias voltage, which can be attributed to the improved photocurrent and the accelerated charge migration under an appropriate bias voltage.[49] Under 0.7 and 1 V, Cr(VI) reduction rates of 100% can be achieved within only 2 h, making the CI-5%-400 amongst the most efficient catalysts for PEC Cr(VI) reduction (Table 1).

Table 1. Comparison of PEC performance of CI-5%-400 with other catalysts.

Preparation method	Reaction time	Photocatalysts	Compounds degraded	Concentration	Catalytic efficiency (%)	Ref.
Microwave-hydrothermal	2h	Co_3O_4/In_2O_3 (CI-5%-400)	Cr(VI)	10 mg/L, 100 mL	PEC 100% after 120 min	This work
hydrothermal	24h	NiFe-LDH/Co_3O_4	Cr(VI)	10 mg/L, 100 mL	PEC 100% after 120 min	29
Electrodeposition and hydrothermal	25h	Ni foam@ZnO@ZnFe-LDH	Cr(VI)	10 mg/L, 100 mL	PEC 96% after 210 min	50
Drop-coating and situ UV reduction	22h	Bi/BiOI-Bi_2O_3	Cr(VI)	10 mg/L,100 mL	PEC 99.5% after 270min	51
Solvothermal	18h	TiO_2	Cr(VI)	2.0μg/mL,50mL	PEC 100% after 180min	52
Hydrothermal	8h	Bi_2MoO_6@Co_3O_4	Reactive bright blue KN-R	60 mg/L, 250mL	PEC 88.43% after 110min	53
Two-step hydrothermal	14h	Co_3O_4@MnO_2	Reactive bright blue KN-R	60 mg/L, 250mL	PEC 94.8% after 120min	54
Anodization and electrodeposition	4h	Co_3O_4/TiO_2–NTs	Methyl orange	4mg/L, 30mL	PEC 90.7% after 600min	20
Electrospinning	25h	In_2O_3/Bi_2MoO_6	4-NP	20mg/L, 40 mL	PEC 95.9% after 240min	55
Precipitation	13h	In_2O_3	MB	20mg/L,50 mL	PEC 95% after 240 min	56

Then the recyclability of the CI-5%-400 was investigated. Although both of 0.7 and 1.0 V are efficient for Cr(VI) reduction, a bias voltage of 0.7 V was selected for further evaluation, in order to minimize the energy consumption and to maximize the economic benefits. As shown in Figure 7B, after five cycles of experiments, the photocatalyst still maintains an efficient catalytic reduction rate of more than 85%, indicating the excellent repeatability and chemical stability of the CI-5%-400 photoelectrode. The slight decrease in the PEC reduction rate may be relevant to the surface deactivation caused by the adsorption of the reduction products of Cr(VI) on the catalyst.[57] Figure S6 shows the Cr 2p XPS spectra of the CI-5%-400 photoelectrode after the PEC performance test. The peaks located at 576.9 and 586.3 eV belong to Cr $2p_{3/2}$ and Cr $2p_{1/2}$ of Cr(III),[58] respectively, confirming the accumulation of Cr(III) on the surface of the catalyst, and the reduction of Cr(VI) to Cr(III) after the PEC reaction.[59]

On the basis of these results, we concluded that the CI-5%-400 is efficient and durable for PEC Cr(VI) reduction. The high activity, robust stability, as well as the facile and rapid synthesis of the CI-5%-400 make it a promising candidate for practical Cr(VI) reduction applications.

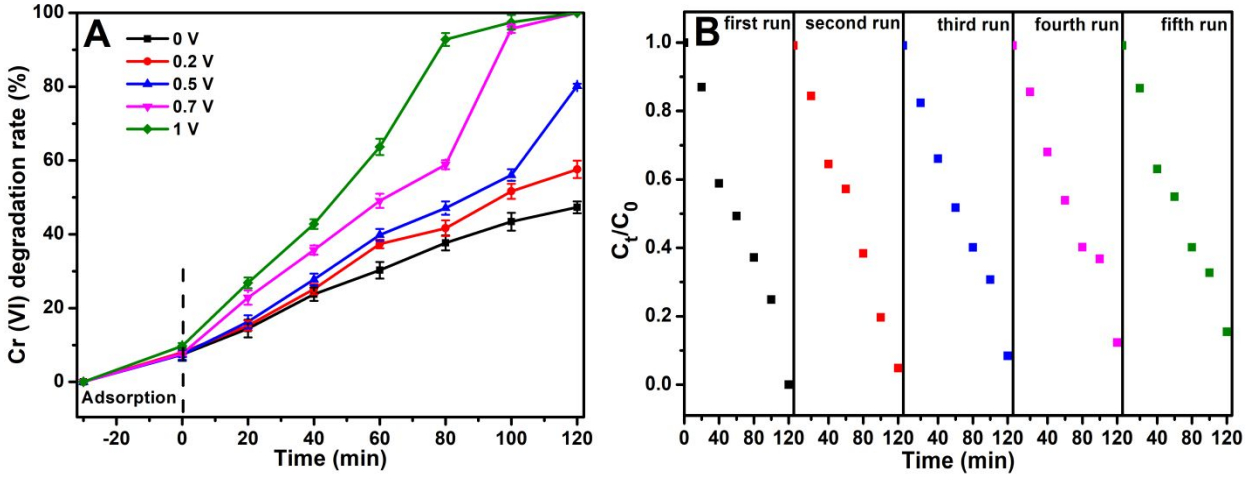

Figure 7. (A) PEC reduction of Cr(VI) by CI-5%-400 composite at different voltages; and (B) Cycling runs for the PEC reduction of Cr(VI) by CI-5%-400.

3.4. Photoelectrocatalytic mechanism

To determine the active species of photoelectrocatalysis, active species trapping experiments were conducted (Figure 8A). Specifically, 1,4-benzoquinone (BQ, 1 mM), isopropyl alcohol (IPA, 1 mM), ethylenediaminetetraacetic acid disodium (EDTA-2Na, 1 mM), and silver nitrate ($AgNO_3$, 0.5 mM)[60] were used as scavengers of superoxide radicals ($\bullet O_2^-$), hydroxyl radicals (•OH), holes (h^+) and electrons (e^-), respectively. As displayed in Figure 8A, the reduction rate of Cr(VI) remained unchanged after the addition of BQ, IPA, and EDTA-2Na. While adding $AgNO_3$ leads to significantly decreased Cr(VI) reduction rates, indicating that photogenerated electrons is the primary active species for Cr(VI) reduction.[61]

To further investigate the electron transfer process, Mott Schottky plots were utilized to determine the flat-band potentials of Co_3O_4, In_2O_3, and CI-5%-400 in 0.1 M Na_2SO_4 electrolyte, as shown in Figure 8B-D. The positive slope in Figure 8B and the negative slope in Figure 8C indicate that In_2O_3 and Co_3O_4 are n-type and p-type semiconductors, respectively. Moreover, the flat-band potentials of In_2O_3 and Co_3O_4 are determined to be -0.63 and 0.34 V (vs. Hg_2Cl_2), respectively. According to the relationship between the conduction band (E_{CB}), flat-band (E_{FB}), and valence band (E_{VB}) potential (For n-type semiconductors, E_{FB} - E_{CB} =0.2 V; For p-type semiconductors, $E_{VB} - E_{FB}$ =0.2 V),[62] the E_{CB} of In_2O_3 and the E_{VB} of Co_3O_4 are calculated to be -0.59 V (vs NHE) and 0.78 V (vs NHE), respectively ($E_{NHE} = E_{SCE} + 0.241$ V).[2] On the other hand, the band gaps (Eg) of Co_3O_4 and In_2O_3 particles obtained from Tauc equation are 1.40 eV

and 2.81 eV (Figure S7), respectively. According to the relationship between Eg, E_{VB}, and E_{CB}, the E_{VB} of In_2O_3 and E_{CB} of Co_3O_4 is calculated to be 2.22 and -0.62 eV, respectively (Eg= E_{VB}-E_{CB}).[63] In addition, the Mott-Schottky plot of the CI-5%-400 composites (Figure 8D) shows a conspicuous "V-shape," indicating the construction of a p-n heterojunction between Co_3O_4 and In_2O_3.[64] According to the energy band classification of heterojunctions,[65] the Co_3O_4/In_2O_3 is a type II heterojunction photocatalyst, which can effectively facilitate the separation of photogenerated carriers.

The energy band structures of n-type In_2O_3 and p-type Co_3O_4 before contact are shown in Figure 9A, and the Cr(VI) reduction process can be expressed by Equation (1-3):

$$Co_3O_4/In_2O_3 + hv \rightarrow e^- + h^+ \quad (1)$$

$$Cr_2O_7^{2-} + 6e^- + 14H^+ \rightarrow 2Cr^{3+} + 7H_2O \quad (2)$$

$$2H_2O + 4h^+ \rightarrow O_2 + 4H^+ \quad (3)$$

The irradiation of visible light leads to the transfer of electrons (e^-) from the CB of Co_3O_4 to the CB of In_2O_3. Meanwhile, the holes (h^+) on the VB of In_2O_3 are transferred to the VB of Co_3O_4 (Eq. (1)). The free e^- from CB then diffuse to the oxide surface, leading to the reduction of the adsorbed $Cr_2O_7^{2-}$, as displayed in Eq. (2). In the meantime, H_2O molecule are oxidized to O_2 by the holes, as shown in Eq. (3). Accordingly, the Cr(VI) reduction mechanism over the CI-5%-400 was proposed, as illustrated in Figure 9B. The VB of Co_3O_4 increases with the increase of Fermi energy, and the CB of In_2O_3 decreases with the decrease of Fermi energy until it reaches equilibrium.[66] Therefore, the p-n heterojunction between Co_3O_4 and In_2O_3 enhances

the migration and separation of photogenerated carriers, effectively improving the PEC activity.

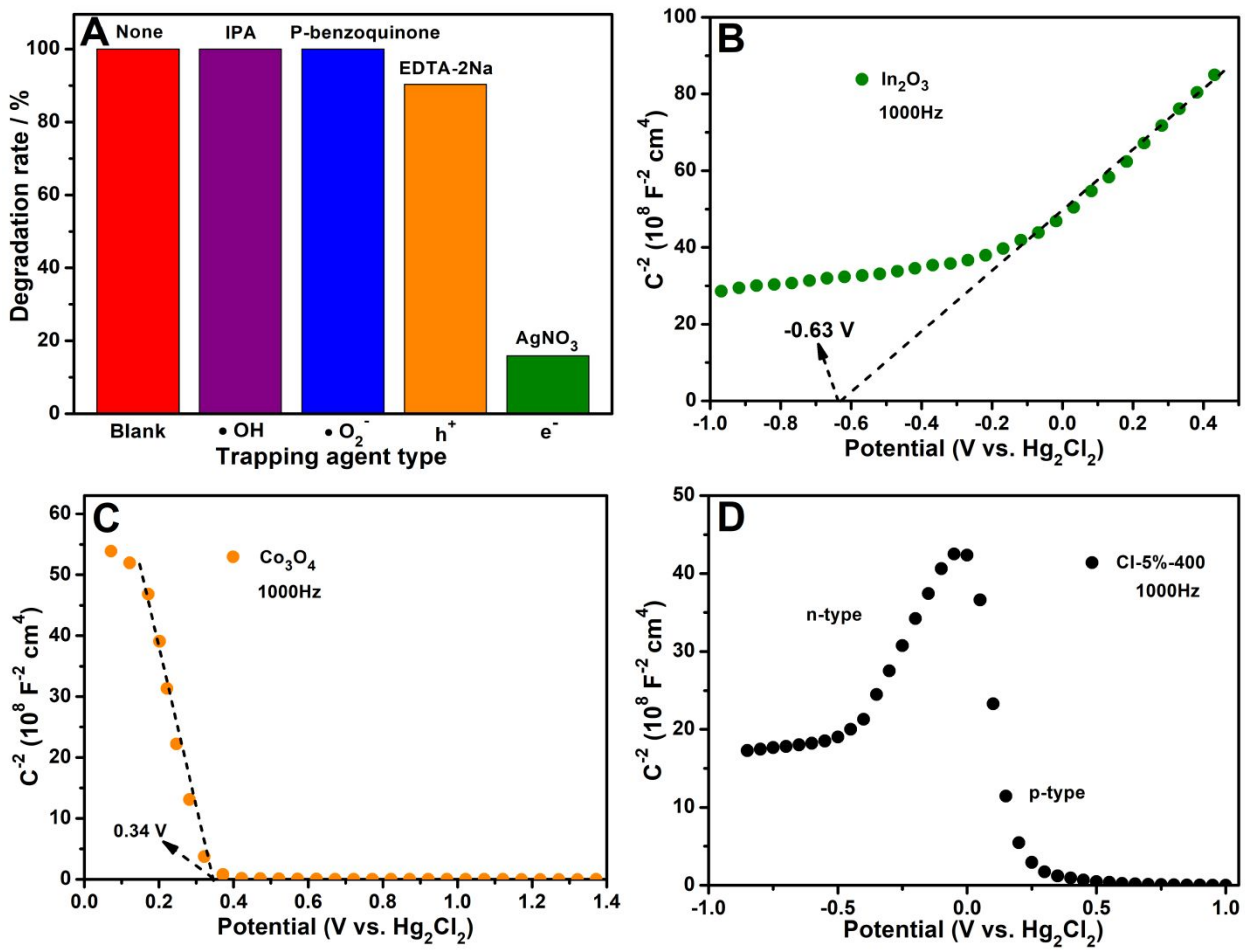

Figure 8. (A) Effect of different scavengers on the PEC reduction of Cr (VI); Mott-Schottky plots of (B) In_2O_3; and (C) Co_3O_4; (D) CI-5%-400.

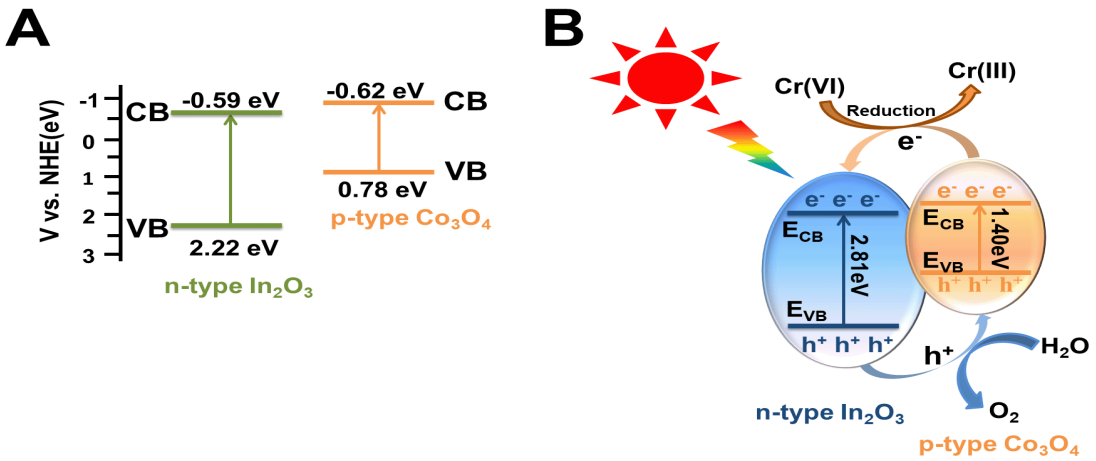

Figure 9. (A) Band structures of n-type In_2O_3 and p-type Co_3O_4 before contact, and (B) schematic diagram of the PEC reduction mechanism of CI-5%-400.

4. Conclusions

In summary, Co_3O_4/In_2O_3 composites with excellent PEC properties were synthesized via a facile microwave-hydrothermal method. The as-prepared CI-5%-400 composite exhibited excellent PEC activity, with a Cr (VI) reduction rate of 100% after 2-h PEC process, exceeding Co_3O_4 and In_2O_3 control samples. PL spectroscopy, transient photocurrent measurements, and EIS analysis demonstrated that the p-n heterojunction between Co_3O_4 and In_2O_3 significantly enhanced the migration and separation of photogenerated electrons and holes. Therefore, Co_3O_4/In_2O_3 composites display a prospective role in an environmental protection.

Supporting Information

Additional experimental details, including materials, characterization methods, photoelectrocatalytic performance tests, and additional tables and figures as mentioned in the text.

Acknowledgements

This work was supported by the Science and Technology Project of Qingdao West Coast New Area (No.2020-91), the Natural Science Foundation of Shandong Province (No. ZR2019BEE075). The authors gratefully acknowledge financial support from Taif University Researchers Supporting Project number (TURSP-2020/135), Taif University, Taif, Saudi Arabia.

References

(1) Xu, D.; Huang, G.; Guo, L.; Chen, Y.; Liu, C. Enhancement of Catalytic Combustion and Thermolysis for Treating Polyethylene Plastic Waste. *Adv. Compos. Hybrid Mater.* **2022**, *5*, 113-129.

(2) Cheng, W.; Wang, Y.; Ge, S.; Ding, X.; Cui, Z.; Shao, Q. One-Step Microwave Hydrothermal Preparation of Cd/Zr-Bimetallic Metal–Organic Frameworks for Enhanced Photochemical Properties. *Adv. Compos. Hybrid Mater.* **2021**, *4*, 150-161.

(3) Gao, S.; Zhao, X.; Fu, Q.; Zhang, T.; Zhu, J.; Hou, F.; Ni, J.; Zhu, C.; Li, T.; Wang, Y.; Murugadoss, V.; Mersal, G. A. M.; Ibrahim, M. M.; El-Bahy, Z. M.; Huang, M.; Guo, Z. Highly Transmitted Silver Nanowires-Swcnts Conductive Flexible Film by Nested Density Structure and Aluminum-Doped Zinc Oxide Capping Layer for Flexible Amorphous Silicon Solar Cells. *J. Mater. Sci. Technol.* **2022**, *126*, 152-160.

(4) Jing, C.; Zhang, Y.; Zheng, J.; Ge, S.; Lin, J.; Pan, D.; Naik, N.; Guo, Z. In-Situ Constructing Visible Light CdS/Cd-MOF Photocatalyst with Enhanced Photodegradation of Methylene Blue. *Particuology* **2022**, *69*, 111-122.

(5) Ouyang, L.; Huang, W.; Huang, M.; Qiu, B. Polyaniline Improves Granulation and Stability of Aerobic Granular Sludge. *Adv. Compos. Hybrid Mater.* **2022**, DOI: 10.1007/s42114-42022-00450-42111.

(6) Deng, Z.; Sun, S.; Li, H.; Pan, D.; Seok, I. Modification of Coconut Shell-Based Activated Carbon and Purification of Wastewater. *Adv. Compos. Hybrid Mater.* **2021**, *4*, 65-73.

(7) Gu, H.; Gao, C.; Zhou, X.; Du, A.; Naik, N.; Guo, Z. Nanocellulose Nanocomposite Aerogel Towards Efficient Oil and Organic Solvent Adsorption. *Adv. Compos. Hybrid Mater.* **2021**, *4*, 459-468.

(8) Guo, L.; Zhang, Y.; Zheng, J.; Shang, L.; Shi, Y.; Wu, Q.; Liu, X.; Wang, Y.; Shi, L.; Shao, Q.

Synthesis and Characterization of Znnicr-Layered Double Hydroxides with High Adsorption Activities for Cr(VI). *Adv. Compos. Hybrid Mater.* **2021**, *4*, 819-829.

(9) Si, Y.; Li, J.; Cui, B.; Tang, D.; Yang, L.; Murugadoss, V.; Maganti, S.; Huang, M.; Guo, Z. Janus Phenol–Formaldehyde Resin and Periodic Mesoporous Organic Silica Nanoadsorbent for the Removal of Heavy Metal Ions and Organic Dyes from Polluted Water. *Adv. Compos. Hybrid Mater.* **2022**, DOI:10.1007/s42114-42022-00446-x.

(10) Paschoal, F. M.; Anderson, M. A.; Zanoni, M. V. Simultaneous Removal of Chromium and Leather Dye from Simulated Tannery Effluent by Photoelectrochemistry. *J. Hazard. Mater.* **2009**, *166*, 531-537.

(11) Fan, Z.; Fang, W.; Zhang, Z.; Chen, M.; Shangguan, W. Highly Active Rod-Like Co_3O_4 Catalyst for the Formaldehyde Oxidation Reaction. *Catal. Commun* **2018**, *103*, 10-14.

(12) Zhang, Y.; Wang, Q.; Lu, J.; Wang, Q.; Cong, Y. Synergistic Photoelectrochemical Reduction of Cr(VI) and Oxidation of Organic Pollutants by G-C_3N_4/TiO_2-NTs Electrodes. *Chemosphere* **2016**, *162*, 55-63.

(13) Li, M.; Li, X.; Jiang, G.; He, G. Hierarchically Macro–Mesoporous ZrO_2–TiO_2 Composites with Enhanced Photocatalytic Activity. *Ceram. Int.* **2015**, *41*, 5749-5757.

(14) Lu, X.; Liu, Z. Efficient All P-Type Heterojunction Photocathodes for Photoelectrochemical Water Splitting. *Dalton Trans.* **2017**, *46*, 7351-7360.

(15) Zheng, Y.; Wang, C.; Li, J.; Zhong, F.; Xiao, Y.; Jiang, L. Enhanced Methane Oxidation over Co_3O_4–In_2O_3-X Composite Oxide Nanoparticles Via Controllable Substitution of Co^{3+}/Co^{2+} by In^{3+} Ions. *ACS Appl. Nano Mater.* **2020**, *3*, 9470-9479.

(16) Yu, L.; Huang, Y.; Xiao, G.; Li, D. Application of Long Wavelength Visible Light (Λ>650 nm) in Photocatalysis with a P-CuO–N-In_2O_3 Quantum Dot Heterojunction Photocatalyst. *J. Mater. Chem. A.* **2013**, *1*, 9637.

(17) Dai, Y.-M.; Lee, W.-I. W.; Lin, W.-C.; Chen, C.-C. Synthesis and Photocatalytic Properties of Nano-Crystalline In_2O_3. *J. Chin. Chem. Soc.* **2013**, *60*, 1415-1424.

(18) Zhang, H.; Liu, W.; Tian, F.; Tang, Z.; Lin, H. The Fabrication of a Co_3O_4/Graphene Oxide (Go)/Polyacrylonitrile (Pan) Nanofiber Membrane for the Degradation of Orange II by Advanced Oxidation Technology. *RSC Adv.* **2019**, *9*, 36517-36523.

(19) Wang, X.; Deng, B.; Yu, L.; Cui, E.; Xiang, Z.; Lu, W. Degradation of Azo Dyes Congo Red by Mnbi Alloy Powders: Performance, Kinetics and Mechanism. *Mater. Chem. Phys.* **2020**, *251*, 123096.

(20) Cao, H.; Lu, Y.; Ning, W.; Zhang, H.; Zheng, G. Co_3o_4 Nanoparticles Modified TiO_2 Nanotube Arrays with Improved Photoelectrochemical Performance. *Russ. J. Appl. Chem.* **2019**, *92*, 64-70.

(21) Akhundi, A.; Habibi-Yangjeh, A. Novel Magnetically Separable G-C_3N_4/AgBr/Fe_3O_4 Nanocomposites as Visible-Light-Driven Photocatalysts with Highly Enhanced Activities. *Ceram. Int.* **2015**, *41*, 5634-5643.

(22) Huang, L.; Li, B.; Su, B.; Xiong, Z.; Zhang, C.; Hou, Y.; Ding, Z.; Wang, S. Fabrication of Hierarchical Co_3O_4@$CdIn_2S_4$ P–N Heterojunction Photocatalysts for Improved CO_2 Reduction with Visible Light. *J. Mater. Chem. A.* **2020**, *8*, 7177-7183.

(23) Shi, S.; Zhang, F.; Lin, H.; Wang, Q.; Shi, E.; Qu, F. Enhanced Triethylamine-Sensing Properties of P-N Heterojunction Co_3O_4/In_2O_3 Hollow Microtubes Derived from Metal–Organic Frameworks. *Sens. Actuators, B.* **2018**, *262*, 739-749.

(24) Lou, Y.; Cao, X. M.; Lan, J.; Wang, L.; Dai, Q.; Guo, Y.; Ma, J.; Zhao, Z.; Guo, Y.; Hu, P.; Lu, G. Ultralow-Temperature Co Oxidation on an In_2O_3-Co_3O_4 Catalyst: A Strategy to Tune Co Adsorption Strength and Oxygen Activation Simultaneously. *Chem. Commun.* **2014**, *50* , 6835-6838.

(25) Yang, B.; Liu, J.; Qin, H.; Liu, Q.; Jing, X.; Zhang, H.; Li, R.; Huang, G.; Wang, J. Co_3O_4 Nanoparticle-Decorated Hierarchical Flower-Like A-Fe_2O_3 Microspheres: Synthesis and Ethanol Sensing Properties. *J. Alloys Compd.* **2017**, *727*, 52-62.

(26) Li, W.; Ma-An, H.; Fu, Y.; Ma, C.; Wang, G.; Dong, X.; Ma, H. Graphene Oxide-Promoted Ti/PbO_2 Photoanode with Photoelectric Synergy Effect for Efficient Photoelectrocatalytic Degradation of Reactive Brilliant Blue. *J. Mater. Sci.* **2020**, *56*, 4741-4752.

(27) Xu, J.; Gao, J.; Liu, Y.; Li, Q.; Wang, L. Fabrication of In_2O_3 /Co_3O_4-Palygorskite Composites by the Pyrolysis of In/Co-MOFs for Efficient Degradation of Methylene Blue and Tetracycline. *Mater. Res. Bull.* **2017**, *91*, 1-8.

(28) Zhao, J.; Ge, S.; Pan, D.; Pan, Y.; Murugadoss, V.; Li, R.; Xie, W.; Lu, Y.; Wu, T.; Wujcik, E. K.; Shao, Q.; Mai, X.; Guo, Z. Microwave Hydrothermal Synthesis of In_2O_3-ZnO Nanocomposites and Their Enhanced Photoelectrochemical Properties. *J. Electrochem. Soc.* **2019**, *166*, H3074-H3083.

(29) Fei, W.; Gao, J.; Li, N.; Chen, D.; Xu, Q.; Li, H.; He, J.; Lu, J. A Visible-Light Active P-N Heterojunction NiFe-LDH/Co_3O_4 Supported on Ni Foam as Photoanode for Photoelectrocatalytic Removal of Contaminants. *J. Hazard. Mater.* **2021**, *402*, 123515.

(30) Abid, H. N.; Nayef, U. M.; Mutlak, F. A. H. Preparation and Characterization Co_3O_4 Nanoparticles on Porous Silicon for Humidity Sensor by Photoluminescence. *Optik* **2019**, *178*, 379-383.

(31) Sun, M.; Li, F.; Su, M.; Wei, D.; Yang, Q.; Yan, T.; Li, D. Fabrication of Mof-Derived Tubular In_2O_3@$SnIn_4S_8$ Hybrid: Heterojunction Formation and Promoted Photocatalytic Reduction of Cr(VI) under Visible Light. *J. Colloid Interface Sci.* **2021**, *596*, 278-287.

(32) Zhang, Q.; Li, W.; Zhao, F.; Xu, C.; Fan, G.; Liu, Q.; Zhang, X.; Zhang, X. Electrochemical Sandwich-Type Thrombin Aptasensor Based on Silver Nanowires& Particles Decorated Electrode and the Signal Amplifier of Pt Loaded Hollow Zinc Ferrite. *Colloids Surf., A* **2021**, *611*, 125804.

(33) Chen, L.; Wang, X.; Rao, Z.; Tang, Z.; Shi, G.; Wang, Y.; Lu, G.; Xie, X.; Chen, D.; Sun, J. One-Pot Synthesis of the MIL-100 (Fe) MOF/MOX Homojunctions with Tunable Hierarchical Pores for the Photocatalytic Removal of BTXS. *Appl. Catal., B* **2022**, *303*, 120885.

(34) Hu, G.; Hu, C.-X.; Zhu, Z.-Y.; Zhang, L.; Wang, Q.; Zhang, H.-L. Construction of Au/CuO/Co_3O_4 Tricomponent Heterojunction Nanotubes for Enhanced Photocatalytic Oxygen Evolution under Visible Light Irradiation. *ACS Sustainable Chem. Eng.* **2018**, *6*, 8801-8808.

(35) Chen, X.; Li, L.; Zhang, W.; Li, Y.; Song, Q.; Zhang, J.; Liu, D. Multi-Pathway Photoelectron Migration in Globular Flower-Like In_2O_3/AgBr/Bi_2WO_6 Synthesized by Microwave-Assisted Method with Enhanced Photocatalytic Activity. *J. Mol. Catal. A: Chem.* **2016**, *414*, 27-36.

(36) Kempasiddaiah, M.; Kandathil, V.; Dateer, R. B.; Baidya, M.; Patil, S. A.; Patil, S. A. Efficient and Recyclable Palladium Enriched Magnetic Nanocatalyst for Reduction of Toxic Environmental Pollutants. *J. Environ. Sci.* **2021**, *101*, 189-204.

(37) Gong, H.; Zhang, X.; Wang, G.; Liu, Y.; Li, Y.; Jin, Z. Dodecahedron ZIF-67 Anchoring ZnCdS Particles for Photocatalytic Hydrogen Evolution. *Mol. Catal.* **2020**, *485*, 110832.

(38) Liu, L.; Ma, H.; Zhang, X.; Wang, G.; Ma, C.; Fu, Y.; Dong, X. Fabrication of Graphene Oxide Wrapped Ti/Co_3O_4 Nanowire Photoanode and Its Superior Photoelectrocatalytic Performance. *Nanotechnology* **2020**, *31*, 225303.

(39) Fan, X.; Xu, Y.; Ma, C.; He, W. In-Situ Growth of Co_3O_4 Nanoparticles Based on Electrospray for an Acetone Gas Sensor. *J. Alloys Compd.* **2021**, *854*, 157234.

(40) Chen, W.; Han, B.; Tian, C.; Liu, X.; Liang, S.; Deng, H.; Lin, Z. MOFs-Derived Ultrathin Holey Co_3O_4 Nanosheets for Enhanced Visible Light CO_2 Reduction. *Appl. Catal., B* **2019**, *244*, 996-1003.

(41) Heidari-Asil, S. A.; Zinatloo-Ajabshir, S.; Amiri, O.; Salavati-Niasari, M. Amino Acid Assisted-Synthesis and Characterization of Magnetically Retrievable $ZnCo_2O_4$–Co_3O_4 Nanostructures as High Activity Visible-Light-Driven Photocatalyst. *Int. J. Hydrogen Energy* **2020**, *45*, 22761-22774.

(42) Wang, Y.; Yu, D.; Wang, W.; Gao, P.; Zhong, S.; Zhang, L.; Zhao, Q.; Liu, B. Synthesizing Co_3O_4-$BiVO_4$/G-C_3N_4 Heterojunction Composites for Superior Photocatalytic Redox Activity. *Sep. Purif. Technol.* **2020**, *239*, 116562.

(43) Hwang, J.; Jung, H.; Shin, H.-S.; Kim, D.-S.; Kim, D. S.; Ju, B.-K.; Chun, M. The Effect of Noble Metals on Co Gas Sensing Properties of In_2O_3 Nanoparticles. *Appl. Sci.* **2021**, *11*, 4903.

(44) Yang, Y.; Cheng, W.; Cheng, Y. F. Preparation of Co_3O_4@ZnO Core-Shell Nanocomposites with Intrinsic P-N Junction as High-Performance Photoelectrodes for Photoelectrochemical Cathodic Protection under Visible Light. *Appl. Surf. Sci.* **2019**, *476*, 815-821.

(45) Peng, H.; Zhang, W.; Song, Y.; Yin, F.; Zhang, C.; Zhang, L. In Situ Construction of Co/Co_3O_4 with N-Doped Porous Carbon as a Bifunctional Electrocatalyst for Oxygen Reduction and Oxygen Evolution

Reactions. *Catal. Today* **2020**, *355*, 286-294.

(46) Chen, K.; Bai, S.; Li, H.; Xue, Y.; Zhang, X.; Liu, M.; Jia, J. The Co_3O_4 Catalyst Derived from Zif-67 and Their Catalytic Performance of Toluene. *Appl. Catal., A* **2020**, *599*, 117614.

(47) Mohamed, R. M.; Ismail, A. A.; Basaleh, A. S.; Bawazir, H. A. Synergistic Impact of Two-Dimensional Ag_2O/Co_3O_4 Nanocomposites for Improved Photocatalytic Performance. *Opt. Mater.* **2022**, *123*, 111937.

(48) Liao, X.; Li, T.-T.; Ren, H.-T.; Mao, Z.; Zhang, X.; Lin, J.-H.; Lou, C.-W. Enhanced Photocatalytic Performance through the Ferroelectric Synergistic Effect of P-N Heterojunction $BiFeO_3/TiO_2$ under Visible-Light Irradiation. *Ceram. Int.* **2021**, *47*, 10786-10795.

(49) Jiang, D.; Du, X.; Chen, D.; Li, Y.; Hao, N.; Qian, J.; Zhong, H.; You, T.; Wang, K. Facile Wet Chemical Method for Fabricating P-Type BiOBr/N-Type Nitrogen Doped Graphene Composites: Efficient Visible-Excited Charge Separation, and High-Performance Photoelectrochemical Sensing. *Carbon* **2016**, *102*, 10-17.

(50) Fei, W.; Song, Y.; Li, N.; Chen, D.; Xu, Q.; Li, H.; He, J.; Lu, J. Fabrication of Visible-Light-Active ZnO/ZnFe-LDH Heterojunction on Ni Foam for Pollutants Removal with Enhanced Photoelectrocatalytic Performance. *Sol. Energy* **2019**, *188*, 593-602.

(51) Wang, Q.; Gao, Q.; Wu, H.; Fan, Y.; Lin, D.; He, Q.; Zhang, Y.; Cong, Y. In Situ Construction of Semimetal Bi Modified $BiOI-Bi_2O_3$ Film with Highly Enhanced Photoelectrocatalytic Performance. *Sep. Purif. Technol.* **2019**, *226*, 232-240.

(52) Zhao, Y.; Chang, W.; Huang, Z.; Feng, X.; Ma, L.; Qi, X.; Li, Z. Enhanced Removal of Toxic Cr(VI) in Tannery Wastewater by Photoelectrocatalysis with Synthetic TiO_2 Hollow Spheres. *Appl. Surf. Sci.* **2017**,

405, 102-110.

(53) Li, H.; Jian, L.; Chen, Y.; Wang, G.; Lyu, J.; Dong, X.; Liu, X.; Ma, H. Fabricating Bi_2MoO_6@Co_3O_4 Core–Shell Heterogeneous Architectures with Z‐Scheme for Superior Photoelectrocatalytic Water Purification. *Chem. Eng. J.* **2022**, *427*, 131716.

(54) Zhao, F.; Song, Y.; Liu, X.; Zhang, X.; Ma, C.; Wang, G.; Fu, Y.; Ma, H. Unraveling Electron-Deficient Setaria-Viridis-Like Co_3O_4@MnO_2 Heterostructure with Superior Photoelectrocatalytic Efficiency for Water Remediation. *Appl. Surf. Sci.* **2022**, *573*, 151473.

(55) Wang, Q.; Lu, Q. Coaxial In_2O_3/Bi_2MoO_6 Heterostructured Nanobelts with Enhanced Photoelectrocatalytic Performance. *J. Nanopart. Res.* **2019**, *21*, 142.

(56) Pan, D.; Ge, S.; Zhang, X.; Mai, X.; Li, S.; Guo, Z. Synthesis and Photoelectrocatalytic Activity of In_2O_3 Hollow Microspheres Via a BiO-Template Route Using Yeast Templates. *Dalton Trans.* **2018**, *47*, 708-715.

(57) Ding, Z.; Liang, J.; Zhang, W.; Wang, W.; Geng, R.; Wang, Y.; Li, P.; Fan, Q. Efficiency and Active Sites of the Synergetic Sorption and Photocatalysis in Cr(VI) Decontamination on a 3D Oxidized Graphene Ribbon Framework. *J. Mater. Chem. A.* **2020**, *8*, 11362-11369.

(58) Kohantorabi, M.; Moussavi, G.; Oulego, P.; Giannakis, S. Synthesis of a Novel, Ternary AgI/CeO_2@G-C_3N_4 Nanocomposite with Exceptional Stability and Reusability for Visible Light-Assisted Photocatalytic Reduction of Hexavalent Chromium. *Appl. Surf. Sci.* **2021**, *555*, 149692.

(59) El-Sheikh, S. M.; Azzam, A. B.; Geioushy, R. A.; El Dars, F. M.; Salah, B. A. Visible-Light-Driven 3d Hierarchical Bi_2S_3/BiOBr Hybrid Structure for Superior Photocatalytic Cr(VI) Reduction. *J. Alloys Compd.*

2021, *857*, 157513.

(60) Li, W.; Li, D.; Lin, Y.; Wang, P.; Chen, W.; Fu, X.; Shao, Y. Evidence for the Active Species Involved in the Photodegradation Process of Methyl Orange on TiO_2. *J. Phys. Chem. C* **2012**, *116*, 3552-3560.

(61) Ren, Z.; Liu, X.; Zhuge, Z.; Gong, Y.; Sun, C. Q. $MoSe_2$/ZnO/ZnSe Hybrids for Efficient Cr(VI) Reduction under Visible Light Irradiation. *Chin. J. Catal.* **2020**, *41*, 180-187.

(62) Li, H.; Wang, G.; Zhang, X.; Jin, Z.. Based on Amorphous Carbon C@$Zn_xCd_{1-X}S/Co_3O_4$ Composite for Efficient Photocatalytic Hydrogen Evolution. *Int. J. Hydrogen Energy* **2020**, *45*, 8405-8417.

(63) Wang, Y.; Liu, X.; Guo, L.; Shang, L.; Ge, S.; Song, G.; Naik, N.; Shao, Q.; Lin, J.; Guo, Z. Metal Organic Framework-Derived C-Doped ZnO/TiO_2 Nanocomposite Catalysts for Enhanced Photodegradation of Rhodamine B. *J. Colloid Interface Sci.* **2021**, *599*, 566-576.

(64) Chen, L.; Xie, X.; Su, T.; Ji, H.; Qin, Z. Co_3O_4/CdS P-N Heterojunction for Enhancing Photocatalytic Hydrogen Production: Co-S Bond as a Bridge for Electron Transfer. *Appl. Surf. Sci.* **2021**, *567*, 150849.

(65) Cheng, T.; Gao, H.; Liu, G.; Pu, Z.; Wang, S.; Yi, Z.; Wu, X.; Yang, H. Preparation of Core-Shell Heterojunction Photocatalysts by Coating CdS Nanoparticles onto $Bi_4Ti_3O_{12}$ Hierarchical Microspheres and Their Photocatalytic Removal of Organic Pollutants and Cr(VI) Ions. *Colloids Surf., A* **2022**, *633*, 127918.

(66) Wan, J.; Xue, P.; Wang, R.; Liu, L.; Liu, E.; Bai, X.; Fan, J.; Hu, X. Synergistic Effects in Simultaneous Photocatalytic Removal of Cr(VI) and Tetracycline Hydrochloride by Z-Scheme Co_3O_4/Ag/Bi_2WO_6 Heterojunction. *Appl. Surf. Sci.* **2019**, *483*, 677-687.

The table of contents entry